A systematic study of proto-neutron star convection in three-dimensional core-collapse supernova simulations

Hiroki Nagakura^{1*}, Adam Burrows¹, David Radice^{2,3}, David Vartanyan⁴

- ¹Department of Astrophysical Sciences, Princeton University, 4 Ivy Lane, Princeton, NJ 08544, USA
- ²Department of Physics, The Pennsylvania State University, University Park, PA 16802, USA
- ³ Department of Astronomy & Astrophysics, The Pennsylvania State University, University Park, PA 16802, USA
- ⁴ Astronomy Department and Theoretical Astrophysics Center, University of California, Berkeley, CA 94720, USA

Accepted XXX. Received YYY; in original form ZZZ

ABSTRACT

This paper presents the first systematic study of proto-neutron star (PNS) convection in three dimensions (3D) based on our latest numerical FORNAX models of core-collapse supernova (CCSN). We confirm that PNS convection commonly occurs, and then quantify the basic physical characteristics of the convection. By virtue of the large number of long-term models, the diversity of PNS convective behavior emerges. We find that the vigor of PNS convection is not correlated with CCSN dynamics at large radii, but rather with the mass of PNS – heavier masses are associated with stronger PNS convection. We find that PNS convection boosts the luminosities of ν_{μ} , ν_{τ} , $\bar{\nu}_{\mu}$, and $\bar{\nu}_{\tau}$ neutrinos, while the impact on other species is complex due to a competition of factors. Finally, we assess the consequent impact on CCSN dynamics and the potential for PNS convection to generate pulsar magnetic fields.

Key words: turbulence - supernovae: general.

1 INTRODUCTION

After years of sustained effort, the core-collapse supernova (CCSN) community has recently fielded three-dimensional (3D) models of CCSN with detailed microphysical inputs and neutrino transport. Progress has been made through increased computational resources and improved numerical algorithms, both of which are still evolving. An important consequence of this progress is that numerous 3D models with varying degrees of sophistication have witnessed shock revival via the neutrino-driven explosion mechanism (Takiwaki et al. 2014; Lentz et al. 2015; Roberts et al. 2016; Gessner & Janka 2018; Ott et al. 2018; Schneider et al. 2019; Glas et al. 2019a; Müller et al. 2019; Vartanyan et al. 2019a; Burrows et al. 2019b; Nagakura et al. 2019a; Burrows et al. 2019a) – the only spherically-symmetric (1D) models that explode are those for very low-mass progenitors (Kitaura et al. 2006; Radice et al. 2017). Among other things, 3D explosion models allow us to quantify the expected observable neutrino and gravitational wave signals, and the detection of those signals will provide vital clues to the explosion mechanism.

Recently, a large number of 3D simulations have become available and they reveal a rich diversity of explosion dynamics and observational signatures (Burrows et al. 2019a;

Vartanyan et al. 2019b; Radice et al. 2019). Low-mass progenitors tend to generate less energetic explosions (at least on average), whereas high-mass progenitors seem to explode more energetically, if the shock is revived and the binding energy of the outer envelope is not too large. However, there are suggestions that some progenitors are less prone to explosion (Pan et al. (2018); Ott et al. (2018); Kuroda et al. (2018); Walk et al. (2019b)). Once it achieves the maximum mass limit, the proto-neutron star (PNS) formed in that context will collapse to a black hole. Whatever happens, the internal dynamical behavior of the event and aspects of the nuclear equation of state (EOS) will be imprinted on its neutrino and gravitational wave signals (Sumiyoshi et al. 2006; Nakamura et al. 2016; Morozova et al. 2018; Torres-Forné et al. 2019; Radice et al. 2019; Sotani & Sumiyoshi 2019). Be that as it may, the large number of 3D CCSN simulations with state-of-the art physics that are emerging in the published literature are opening a new window into the explodability and observational signals of massive stars.

The physics of inner PNS convection has been studied for many years (Dessart et al. 2006) and is one of the key elements of CCSN theory. Such convection appears in the inner regions ($10 \lesssim r \lesssim 25$ km) of the PNS and persists whether the shock wave is revived or not – it is a generic feature in all stellar collapse scenarios. It is driven predominantly by negative lepton gradients that are a consequence of net and persistent electron-neutrino loss and is sustained un-

^{*} E-mail: hirokin@astro.princeton.edu

til the PNS has almost fully deleptonized and cooled many seconds after bounce (Burrows & Lattimer 1986; Roberts et al. 2012). This characteristic timescale is much longer that the dynamical timescale of the PNS (~1 ms), and the PNS evolves quasi-hydrostatically. Though neutrino-driven convection behind the shock has in the past been studied as a possible agency and site for the dynamo origin of pulsar magnetism (Thompson & Duncan 1993; Bonanno et al. 2006), PNS convection in the inner region is also a possible context for dynamo action and magnetic field generation. This possibility, that pulsar B-fields are sourced in the inner proto-neutron star, is one motivation for the closer look at the physics and phenomena that accompany PNS convection represented by this paper.

Moreover, the role of PNS convection on CCSN dynamics is still an open question. In earlier studies, it was suggested that it played a direct role in the explosion mechanism (Epstein 1979; Bruenn et al. 1979; Livio et al. 1980). PNS convection was supposed to generate large-scale overturn, significantly enhancing neutrino fluxes and dramatically increasing neutrino heating in the outer gain region. However, as pointed out by Lattimer & Mazurek (1981) and Burrows & Lattimer (1988), the positive entropy gradient, which coexists with the negative lepton gradient in the envelope of the PNS, stabilizes convection there and suppresses largescale overturn. Furthermore, Burrows et al. (1995) observed neither large-scale overturn, nor enhancement of neutrino luminosities, in their axisymmetric simulations. On the other hand, Keil et al. (1996) found that PNS convection increases both neutrino luminosities and the average neutrino energies by factors of ~ 2 and $\sim 10\%$, respectively, compared with spherically-symmetric models. It should be noted, however, that those numerical simulations employed a crude gray approximation to neutrino transport and this is likely a crucial deficit. Indeed, Mezzacappa et al. (1998) suggested that the growth of PNS convection is delayed when a better treatment of neutrino transport is employed, suggesting that the treatment of neutrino transport may change the characteristics of PNS convection.

Detailed multi-group studies of PNS convection in axisymmetry were conducted by Dessart et al. (2006) and Buras et al. (2006). The former showed that the effect of PNS convection on neutrino emission depends upon neutrino species; $\bar{\nu}_e$ (electron-type anti-neutrino) and ν_x (heavy-leptonic neutrino) luminosities were roughly $\gtrsim 15\%$ and $\gtrsim 30\%$ higher, respectively, than those in sphericallysymmetric models and ν_e (electron-type neutrino) emissions were less sensitive to PNS convection. However, the latter study suggested that the neutrino luminosities of all species are enhanced by PNS convection. In addition, it has recently been suggested that PNS convection could influence shock revival by the generation of outgoing hydrodynamic waves (Gossan et al. 2019), contributing perhaps $\sim 10\%$ to the power deposition behind the shock. It should be noted, however, that sound waves generated by infalling matter plumes that impinge upon the PNS, could be equally in play, though both processes are likely subdominant. To be sure, these mechanisms remain to be adequately quantified.

In this paper, we present results of the first systematic study, across a broad range of massive-star progenitors and supernova models, of PNS convection using the results of state-of-the art 3D CCSN simulations. A few pre-

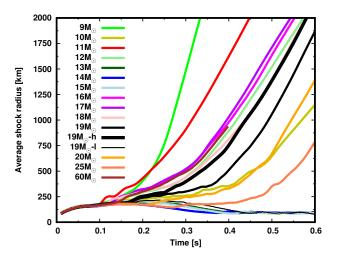


Figure 1. The time evolution of the mean shock radius. Color denotes the ZAMS mass of the progenitor. For the $19-M_{\odot}$ model (black line), the results of high and low resolution models are displayed as thicker and thinner lines, respectively, than the line denoting the standard resolution model.

vious studies addressed PNS convection in 3D (Glas et al. 2019b; Walk et al. 2019a; Powell & Müller 2019), but they were limited to a few models. Moreover, those studies generally focused on the relation between PNS convection and the lepton-emission self-sustained asymmetry (LESA) phenomenon (Tamborra et al. 2014; O'Connor & Couch 2018; Vartanyan et al. 2019b)) or gravitational radiation (Powell & Müller 2019). In this study, we integrate the results of sixteen 3D CCSN simulations computed by Fornax (Burrows et al. 2019a). By using a large number of models, we address the following fundamental questions in PNS convection: what is the progenitor dependence?; are there any qualitative differences between exploding and non-exploding models?; and what are the dynamical features of PNS convection? In addressing these issues, we quantify the basic characteristics and consequences of PNS convection. In Sec. 2, we briefly summarize our 3D numerical CCSN models. We present the results of our analyses in Sec. 3. This is the core of the paper. Finally, we summarize and discuss our results in Sec. 4. We stress that PNS convection is not the "neutron-finger" convection posited by J. Wilson (Bethe & Wilson 1985; Wilson & Mayle 1988). Such doublydiffusive instabilities have been shown not to arise in the supernova context (Bruenn & Dineva 1996; Dessart et al. 2006). Rather, this is classic Ledoux convection, but in the exotic environment of the PNS core.

2 METHOD AND MODEL

All 3D CCSN simulations presented in this paper were carried out using our 3D neutrino-radiation hydrodynamic code, FORNAX. The details of the methodology and basic equations and code tests can be found in a series of our previous papers (Skinner et al. 2016; Radice et al. 2017; Vartanyan et al. 2018; Skinner et al. 2019). We also direct the reader to Burrows et al. (2019a) for a discussion of the input physics and numerical setups employed. Here, we highlight

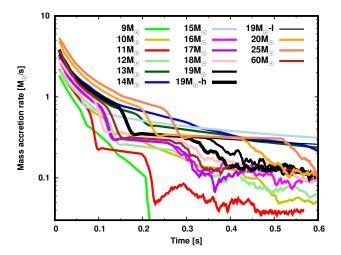


Figure 2. The time evolution of the mass accretion rate measured at 500 km for all 3D models presented in this paper.

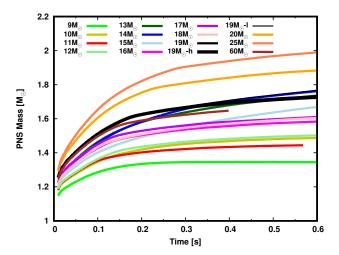


Figure 3. The time evolution of the mass of the PNS, which is defined as the enclosed baryon mass up to a radius at which the angle-averaged mass density (ρ_{ave}) is 10^{11}g/cm^3 . As discussed in the body of the text, the mass of the PNS has a clear correlation with the vigor of PNS convection (see, e.g., Fig. 10).

the results for fourteen solar-metallicity, non-rotating CCSN progenitors with zero-age-main sequence (ZAMS) masses from 9 to $20\,M_{\odot}$, taken from Sukhbold et al. (2016). We also include a $60\,M_{\odot}$ progenitor from the same reference and the $25 M_{\odot}$ model from Sukhbold et al. (2018). We start all simulations in spherically symmetry and map them to 3D at 10ms after core bounce, adding very modest velocity perturbations (with maximum speed 100 km/s), following the prescription detailed in Müller & Janka (2015). We adopt spherical coordinates out to 20,000 km from the stellar center by deploying $678(r) \times 128(\theta) \times 256(\phi)$ grid points as our standard resolution. We also consider high- and lowresolution simulations of the $19\,M_{\odot}$ progenitor, in which the angular resolution in the θ and ϕ directions is higher and lower by a factor of two than the default (Nagakura et al. 2019a). Therefore, in total, we consider sixteen CCSN

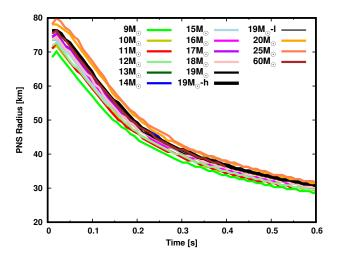


Figure 4. The time evolution of the PNS radius, defined at the radius where $\rho = 10^{11} \mathrm{g/cm^3}$ on average.

models in this study. We use a common spatial grid for the hydrodynamics and the neutrino transport. For the latter, we employ 12 energy groups and three neutrino species are distinguished: ν_e , $\bar{\nu}_e$, and ν_x . Note that we assume that all heavy leptonic neutrinos and their anti-partners have the same distribution functions.

The detailed analyses of the explodability and of the observable characteristics imprinted in gravitational waves and neutrinos of these models can be found in Burrows et al. (2019a), Radice et al. (2019) and Vartanyan et al. (2019b). As shown in Fig. 1, the majority of our models explode, but our current 3D models with 13–,14– and 15 M_{\odot} progenitors and our low-resolution model of the 19 M_{\odot} progenitor do not by the end of those simulations. We note that the 19 M_{\odot} models with standard and higher angular resolutions experienced shock revival, the higher-resolution model experiencing more vigorous shock expansion than that of the standard resolution (see the thick black line in Fig. 1). Also, as we show in §3, the different 19 M_{\odot} models provide insight into the potential effect of shock revival on PNS convection.

In support of our general description of PNS convection, we provide the time evolution of the mass-accretion rates (Fig. 2), PNS masses (Fig. 3), and PNS radii (Fig. 4). These plots support our description of PNS convection and its systematics with progenitor. One of remarkable trend is that the mass accretion rate of the $25\,M_\odot$ and $9\,M_\odot$ models is the highest and lowest, respectively, among all models, the PNS mass recapitulates this trend, and that the PNS radius trends similarly, though with a smaller spread. We show in the next section that the vigor of PNS convection correlates closely with PNS mass, whereas the dependence of PNS convection overall on explodability, mass accretion rate, and PNS radius is weaker.

3 RESULTS

In this section, we present our central results. In §3.2, after describing the basic characteristics of PNS convection, we delve into the diversity with progenitor. In §3.3, we analyze

the characteristics of the turbulence in PNS convection. Finally, in §3.4 we discuss the impact of PNS convection on neutrino emissions.

3.1 Basic characteristics of PNS convection

Figure 5 displays radial distributions of the angle-averaged speed of non-radial, transverse fluid motions (V_{tan}) for all models as a function of time in the region bounded by $10 \lesssim r \lesssim 25$ km in which PNS convection is manifest and for which $V_{\rm tan} \gtrsim 10^8$ km/s. PNS convection commences $\lesssim 50$ ms after bounce and is sustained during the rest of the postbounce phase. The Mach number associated with the convective motion is an order of $\sim 10^{-2}$, which is of the same order as that found in previous 2D simulations (Dessart et al. 2006; Buras et al. 2006). Commonly, the convective layer moves inward with time in accordance with PNS contraction. We observe that the convective layer resides between the two isodensity surfaces 10^{13} and 10^{14} g/cm³, except during the very early post-bounce phase. The spatial width of this convective layer is ~ 10 km and is almost constant with time in our simulations¹. The characteristic frequencies of PNS convection can be estimated as

$$f \sim \frac{V_{\rm tan}\ell}{\pi R} \sim 100 \ \left(\frac{V_{\rm tan}}{2\times 10^8 {\rm cm/s}}\right) \ \left(\frac{\ell}{10}\right) \ \left(\frac{R}{20 {\rm km}}\right)^{-1} \ [{\rm Hz}] \ , \quad (1) \\ {\rm We \ now \ turn \ our \ attention \ to \ a \ more \ quantitative \ discussion}$$

where R and ℓ denote the mean radius of PNS convection and the spherical harmonic index, respectively. Note that ℓ is associated with the size of an eddy in the convective layer, which is induced in the non-linear phase by the turbulent cascade (see §3.3). The small eddy motions are responsible for the higher frequencies. The corresponding characteristic timescales range from ~ 3 ms to ~ 20 ms.

We confirm that there is an annulus of weak non-radial motions in the region between the two isodensity surfaces at 10^{12} and 10^{13} g/cm³, where the positive radial gradient in the entropy suppresses large-scale overturn (see also Fig. 7). The convectively stable layer is also observed in the Y_e distributions, which are displayed in Fig. 6. The magnitude of the Y_e fluctuations in the convective layer are $\sim 10\%$, but such fluctuations are muted in the convectively stable region.

Figure 7 portrays the radial profiles of the angleaveraged electron fraction (Y_e) and entropy per baryon (S)at two different time snapshots: 200 ms and 500 ms after bounce. Those distributions deep inside the PNS core $(r \lesssim 10 \text{km})$ are approximately universal among the progenitors (Bruenn 1985; Lattimer & Prakash 2000; Liebendörfer et al. 2003). Such behavior is consistent with both 1) the universal dynamics of the inner core during the collapse phase, in which both Y_e and entropy distributions are self-regulated by electron-capture reactions (Nagakura et al. 2019b) and 2) to the fact that the timescale of neutrino diffusion inside the PNS core is of order seconds and the changes in Y_e and entropy are nearly identical (Nagakura et al. 2019b). The inner Y_e and entropy distributions in the PNS convective layer are qualitatively similar from model to model. One of

the salient (and expected) characteristics of these 3D radial profiles is that they are flat in the convective layer. This is particularly true for the entropy profile, and is in sharp contrast with what obtains in spherically-symmetric models. Moreover, PNS convection dredges up the surface matter of the PNS core, and thereby smoothes the otherwise sharp bumps in the radial profile of Y_e . It should be noted, however, that the Y_e gradient on the outside of the PNS is still negative, and this continues to drive PNS convection. The negative Y_e gradient is sustained by lepton-loss at the outer edge of the convective layer, in particular by lower-energy ν_e s that have smaller interaction cross-sections.

We find that the convectively unstable region is always wider than the unstable regions in 1D. There are several reasons for this difference: 1) convective overshoot and the turbulent pressure, both of which enlarge the convective layer, are artificially suppressed in 1D; and 2) PNS expansion due to the accelerated deleptonization by PNS convection is suppressed in 1D (Buras et al. 2006). In fact, the PNS radius is consistently larger in 3D than in 1D (Fig. 8). These characteristics also affect the progenitor dependence of PNS convection, which is discussed next.

Progenitor dependence of PNS convection

of the diversity observed in PNS convection. Importantly, we find that low-mass progenitor models tend to have more quiet PNS convection. Indeed, the $9 M_{\odot}$ model, which is the lowest ZAMS mass model among our model suite, has the weakest PNS convection (Figure 5). Such a correlation between the ZAMS mass and the vigor of PNS convection is, however, not rigorously monotonic. For instance, the $10 M_{\odot}$ model experiences a bit stronger convection than found in the $11 M_{\odot}$ model.

The $20 M_{\odot}$ and $25 M_{\odot}$ models, on the other hand, have wider and more vigorous convective layers than found in the other models. Generally, models with wider convective zones experience more vigorous PNS convection. This can be clearly seen by comparing the maximum tangential velocities in the region of PNS convection among models (Fig. 9). The $20\,M_{\bigodot}$ and $25\,M_{\bigodot}$ models have faster non-radial motions than the others. We reiterate that the $9 M_{\odot}$ model has the lowest transverse convective speeds. The ratio of the maximum tangential velocity for the strongest and the weakest models is roughly a factor of 4, which indicates that the kinetic energy in the convective layer varies by more than an order of magnitude. As shown in Fig. 10, the total kinetic energy of PNS convection is roughly a few 10^{49} erg but it can exceeds 10^{50} erg for the most convective models.

We find that the vigor of PNS convection accounts in part for the difference among models in the Y_e distributions (Figures 6 and 7). Convection dredges up Y_e -rich matter inside the PNS core and carries the lepton-number outward via large eddies. This process works more efficiently in the stronger convective context and results in higher lepton number flux (see §3.4) and higher Y_e s in the outer PNS (due to the consequent increase in the absorption of ν_e by free neutrons).

Here, we briefly remark on the resolution dependence (Nagakura et al. 2019a). Comparing three $19 M_{\odot}$ models, we find that the general vigor of PNS convection is not very

¹ Note that the inner boundary of the convective layer sinks further inside the PNS core in the later phase and that the entire core will eventually become convective. This happens on the timescale of roughly a few seconds (Roberts et al. 2012).

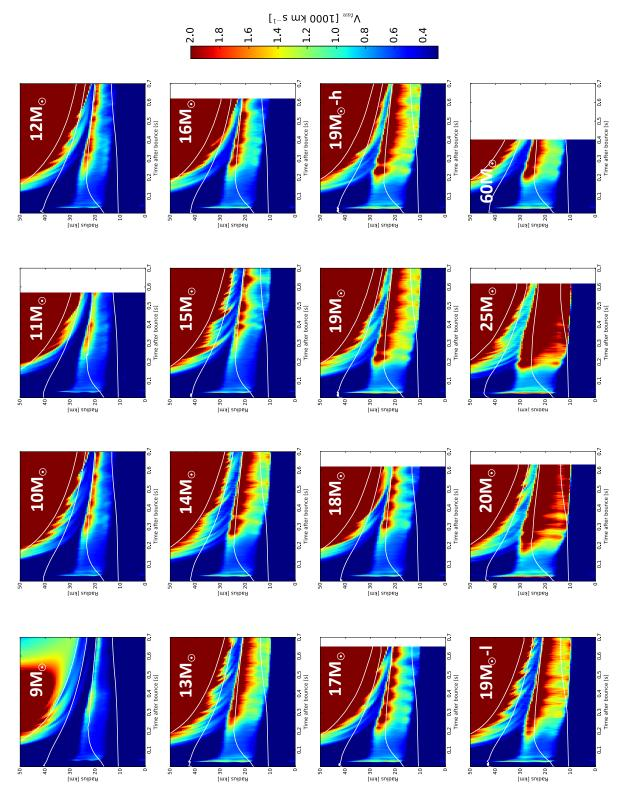


Figure 5. Radius-time diagrams of the angle-averaged speed of non-radial fluid motions (Vtan) in the inner 50 km through 0.7 s. Models terminated before 0.7s contain blank white space from the time at the end of the simulation to 0.7s. In each panel, there are two regions with high V_{tan} (brown), but only the bottom one corresponds to the region experiencing PNS convection. The other regions are the base of the outer convective zone driven by neutrino heating from below. On each colormap as white lines, we also display angled-average isodensity radii, delineating 10^{11} , 10^{12} , 10^{13} and 10^{14} g/cm³, respectively.

sensitive to resolution. More quantitatively, however, our low-resolution $19\,M_{\odot}$ model experiences slightly stronger convection than the higher-resolution model. It should be noted that the lowest resolution $19\,M_{\odot}$ model does not explode and continues to accrete matter. However, the other

non-exploding models, the 13–, 14– and 15 – M_{\odot} models, do not in any obvious way, despite their shared outcome, share any obvious features with the 19 M_{\odot} models.

Indeed, we find that the baryon mass of the PNS is the most important determinant of the vigor of PNS con-

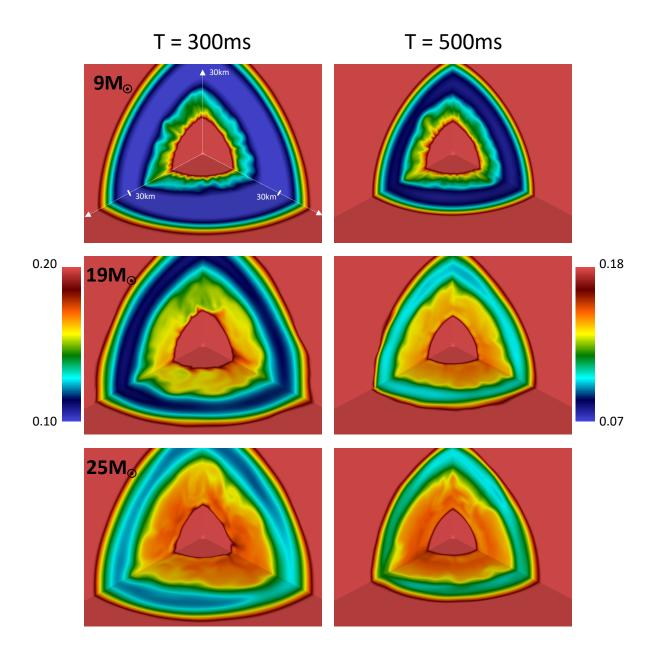


Figure 6. 3D color maps of the Y_e distributions in the vicinity of PNS. The left and right panels correspond to post-bounce times of $t=300 \mathrm{ms}$ and $t=500 \mathrm{ms}$, respectively. From top to bottom, the results for the 9-,19- and $25-M_{\odot}$ models are displayed.

vection. This trend can be seen by comparing two figures, Figs. 3 and 10, in which stronger convection is seen to be generated in models with a higher PNS mass². This is more clearly shown in Fig. 12, which compares for the various progenitors the PNS mass and the transverse turbulent kinetic energy in the convective region at T=400 and 500 ms after bounce. Consistently, models with vigorous convection tends to have higher baryon masses in the convective layer itself (varying roughly by a factor of ~ 2 ; see Fig. 11). Of

course, the mass difference enhances the spread in the kinetic energy of PNS motions between strongly and weakly convective proto-neutron stars (Fig. 10).

The correlation between PNS mass and the vigor of PNS convection is one of the most important findings in this paper. It is in part a consequence of the deeper gravitational potential well in models with a heavier PNS mass, which thereby accelerates eddy motions. In addition, the accelerated eddies induce stronger overshooting that expands the convective layer, consistent with the trend seen in Fig. 5. Note also that this is consistent with what we find in the resolution dependence of PNS convection for $19\,M_{\odot}$ mod-

 $^{^2}$ Note that the total mass of the PNS is here defined as the mass enclosed by an isodensity surface with $\rho=10^{11} \rm g/cm^3.$

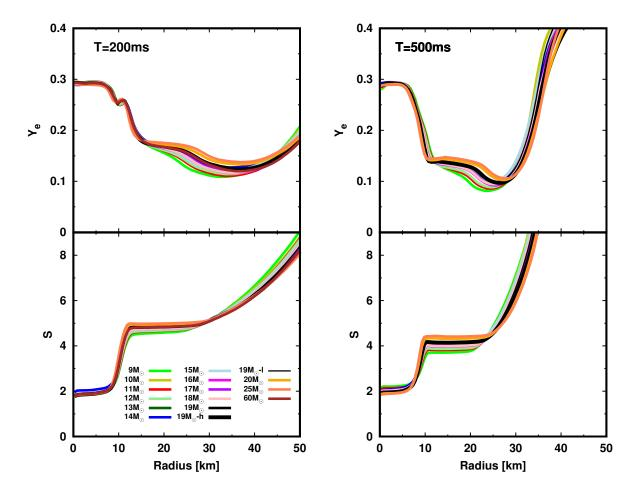


Figure 7. Radial profiles of angle-averaged electron fraction (Y_e) on top and entropy per baryon (S) on bottom panels at 200 ms (left panel) and 500 ms (right panel) after bounce, respectively. On the right panel, we do not include the $60 M_{\odot}$ model.

els; the low-resolution model experiences a bit stronger PNS convection than the others. The failure of the shock to explode in the low-resolution model results in greater ongoing mass accretion onto the PNS core, and, thus, a slightly more massive PNS. The correlation of PNS mass and average accretion rate with the vigor of PNS convection is a useful means with which to analyze the progenitor dependence of PNS convection.

3.3 Turbulence in PNS convection

We observe that PNS convection starts near $\lesssim 50$ ms after bounce and is sustained for the rest of the post-bounce phase. Convective motions grow rapidly, quickly transitioning to the non-linear turbulent phase. However, the spectrum of turbulence in PNS convection is not described by the simple Kolmogorov power-law. We here characterize the turbulent flow in PNS convection and then discuss its progenitor dependence.

Figure 13 displays X-Z plane slice color maps of the Y_e distributions, superposing fluid velocity vector fields. We observe that the inhomogeneities in Y_e coincide with the eddy structure traced by the vector fields. In the linear phase of PNS convection, high- Y_e bubbles move upward from the surface of the PNS core (~ 10 km) and low- Y_e structures sink down from the outer edge of the convective layer. Both flows reflect at the convective boundaries and execute circular motions. This results in a maximum curvature radius for the eddies equal to roughly the half width of the convective layer. Once the convection becomes non-linear, smaller eddies emerge through the collision of larger eddies. Such dynamics is consistent with the classical process of the turbulent cascade.

As an aside, we remark on what Figure 13 suggests about the LESA. As shown, a large-scale (dipole) asymmetry in the Y_e distribution is clearly seen in the 9- and $19-M_{\odot}$ models, associated with what we observed earlier in our published models (Vartanyan et al. 2019b). However, contrary to the previous claim concerning the possible physical origin of the LESA phenomenon by Glas et al. (2019b), we do not observe concomitant large-scale coherent matter motions in the envelope of the PNS. It should be noted that large-scale coherent motions can be triggered by the random breaking of global symmetry in the shocked envelope, not necessarily first in the PNS convective zone, and that asymmetries in the latter might be a consequence of the former. Moreover, such symmetry breaking might be correlated with the PNS kick direction, as suggested by Nagakura et al. (2019c). In-

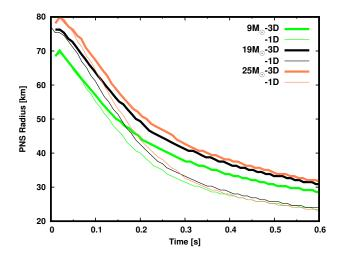


Figure 8. Comparison of the time evolution of the PNS radius between 3D (thick lines) and 1D (thin lines) models for the three representative models.

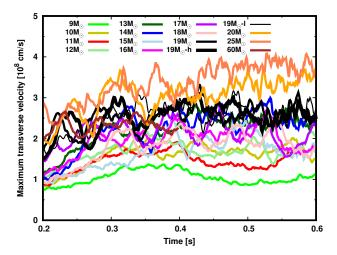


Figure 9. Time evolution of the maximum tangential velocity in the region of PNS convection.

deed, PNS proper motion should be a generic outcome of a broken symmetry which might be connected to the LESA direction and/or the vector dipole direction of the exploding shock (Vartanyan et al. 2019b). However, we suggest that a comprehensive understanding of the origin of the LESA, its direction, and potential correlations with the vector directions of other phenomena has yet to be found and we will leave this topic to future work.

To investigate the turbulent state of PNS convection, we compute the turbulent kinetic energy spectrum as a function of spherical-harmonics index ℓ at three different times; the results are displayed in Fig. 14. We use the formalism of Abdikamalov et al. (2015), but the region sampled and averaged is between two isodensity surfaces: 10^{13} and 10^{14} g/cm³. As displayed in this figure, the spectra obey a broken power-law, which indicates that smaller eddies are actually created in the non-linear phase. It should be noted, however, that the spectra deviate from Kolmogorov's theory. Indeed,

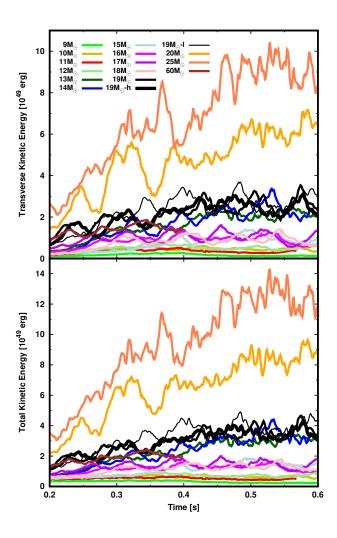


Figure 10. Time evolution of the transverse (upper) and total (bottom) kinetic energy of PNS convection for the 3D models of this study.

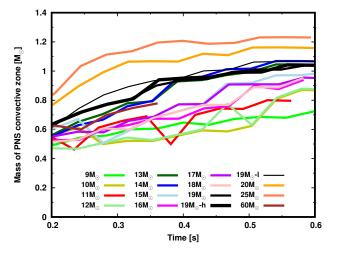


Figure 11. The time evolution of the baryon mass for all models in the region of PNS convection. See text for a discussion.

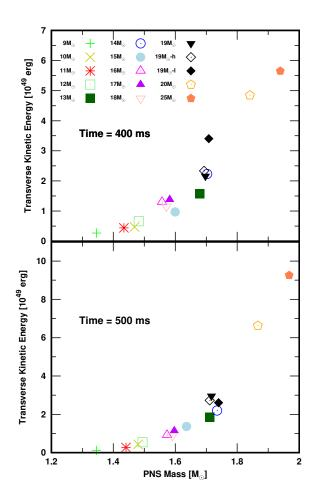


Figure 12. PNS mass vs. the transverse kinetic energy of PNS convection. The upper and lower panels are for T=400 and 500 ms, respectively, after bounce. The $60M_{\odot}$ model is not included in these plots.

they decline more sharply than $\ell^{-\frac{3}{5}}$ at $\ell > 10$. This behavior seems not due to numerical resolution, since there are no remarkable differences in the spectra for the three different resolution models of the $19 M_{\odot}$ progenitor (Nagakura et al. 2019a). In addition, we find that the spectrum at lower ℓs ($\ell \lesssim 10$) strongly varies with progenitor. Models with stronger PNS convection tend to evince a sharper decline in the spectrum - turbulent kinetic energy accumulates in the large eddies. Some possible explanation for this tendency might be found by observing the systematics of PNS convection with radial width. As mentioned already, models with stronger PNS convection tend to have convective layers with wider radial widths (Fig. 5), which results in expanding the maximum eddy scale in the convective region. As a result, stronger convection generates larger eddies more efficiently. The deviation from the Kolmogorov's cascade at higher $\ell(>10)$ may also imply that momentum transfer by neutrinos, or neutrino-drag, affects the spectrum. Indeed, neutrino diffusion is more efficient for smaller eddies, i.e., the effects of neutrino viscosity are greater for smaller eddies (van den Horn & van Weert 1984; Burrows & Lattimer 1988; Thompson & Duncan 1993; Guilet et al. 2015; Melson & Janka 2019). We also note that the small to modest aspect ratio of the convective region may result in a quasi-2D cascade, i.e. inverse from small to large scales. However, we don't yet feel comfortable, in lieu of even higher resolution studies, highlighting this possibility at this time.

In Fig. 15, we provide angular maps of the turbulent energy flux (kinetic and thermal energy flux) in the PNS zone. Note that the total energy flux is dominated by the thermal contribution, This is consistent with the fact that the turbulent Mach number in PNS convection is less than 10%, i.e., the kinetic energy is less than a few % (§3.1). In Fig. 15, a Mollweide projection of the turbulent energy flux at 300 ms after core bounce is displayed. This is computed at the isodensity surface where the matter density is 5×10^{13} g/cm³, which is roughly located in the middle of the convective layer. As shown in the figure, when overall PNS convection is stronger, there are higher angular variations. Indeed, the $25\,M_{\odot}$ model has the strongest color contrast of all the maps, while the $9 M_{\odot}$ model has the weakest contrast. These figures also clearly indicate that models with stronger PNS convection have larger scale variations in the angular directions. This is consistent with our finding that the turbulent-kinetic-energy spectra at lower \(\ell \)s possess significantly higher energies than at higher ℓ s (Fig. 14).

Figure 16 of the angle-averaged turbulent energy flux at three different time snapshots clearly shows that PNS convection commonly generates net outgoing energy fluxes. This is not a trivial outcome and could be of relevance in the possible generation of hydrodynamic waves (Gossan et al. 2019). Indeed, as Fig. 15 demonstrates, incoming energy flux dominates outgoing flux at some angular points. The dominance of the outgoing energy flux indicates that energy transport by buoyancy is more efficient than that by downflows from the outer edge of the convective layer. This is in part due to the inhomogeneous matter distributions in background flows, when there is a strong negative density gradient in the convective layer. The thermal enthalpy is also higher at smaller radii, indicating that energy transport by buoyant motions is larger than that of downflows. It is also important to mention that the energy flux is time-dependent and that the peak flux grows with time for the duration of our simulations. In accordance with the PNS contraction, the radial width of the outgoing flux also changes. We note that in the turbulent gain region before explosion, the corresponding net turbulent energy flux is negative, not positive. This significant difference is due to the modest-to-large post-shock accretion/infall speeds behind the shock as the accreted matter settles onto the inner core. This difference highlights one important distinct characteristic of PNS convection - it is in a truly "stellar" convective zone in the classic stellar evolution sense.

Figure 16 also suggests that models with stronger PNS convection manifest higher angle-averaged turbulent energy flux. Indeed, the $25\,M_{\odot}$ model has the highest peak turbulent energy flux. To further buttress our argument that the PNS mass and the vigor of PNS convection are correlated, we compare the PNS mass and the peak angle-averaged turbulent energy flux in Fig. 17. This figure clearly displays this positive correlation and lends confidence to our finding that the PNS mass is an important determinant of the vigor of PNS convection.

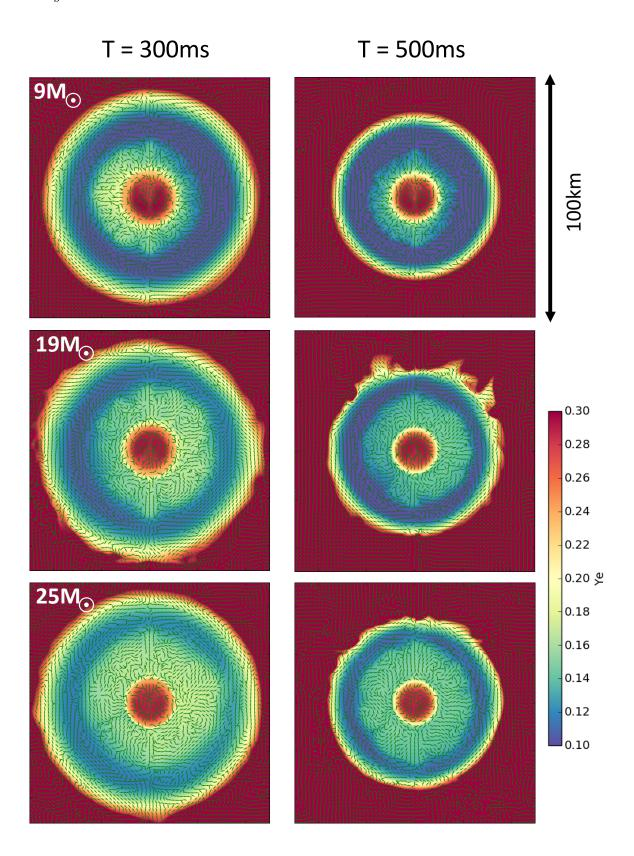


Figure 13. Two dimensional (X-Z) slice map of Y_e in color, with fluid motions as vectors. Note that the length of each velocity vector is forced to be the same. The models and times shown are the same as in Fig. 6.

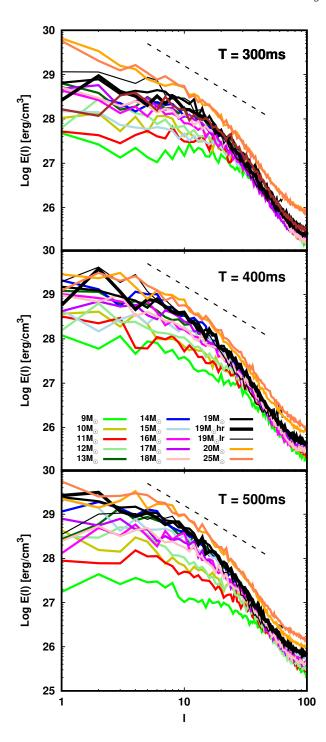


Figure 14. The power spectrum of the transverse kinetic energy density versus spherical harmonic index (ℓ) . It is computed and averaged in the region between two isodensity surfaces, 10^{13} and 10^{14} g/cm³, which roughly corresponds to the PNS convective layer (Fig. 5). The power spectrum is averaged in time over an interval of 10 ms. Note that we do not include the result for the $60\,M_{\odot}$ model, except for the time snapshot at T=300 ms after bounce (top panel), since that simulation was terminated before T=400 ms. The dashed line has a slope of $-\frac{5}{3}$ so as to compare with a Kolmogorov spectrum.

3.4 Neutrino emissions

The effect of PNS convection on neutrino emissions is one of the fundamental issues in CCSN theory. We focus in our analysis on a subset of representative progenitors and compare our 3D results with the results for corresponding spherically-symmetric simulations to quantify the impact of PNS convection.

First, we consider the effect of PNS convection on deleptonization. Fig. 18 displays radial profiles of angle-average Y_e distributions for three selected progenitors (9-, 19-, and $25 - M_{\odot}$) as a function of interior baryon mass coordinate³. As shown in the figure, Y_e at $M \gtrsim 0.4 M_{\odot}$ is quite different from that for the spherically-symmetric simulations. In the vicinity of the inner edge of the convective layer Y_e is systematically smaller in 3D than in 1D, whereas there is the opposite behavior at the outer edge. This is evidence that PNS convection carries the leptons (mainly electrons) from the inside to the outside of the convective zone. In addition, we find that the total electron number inside the PNS is smaller in 3D than in 1D⁴, i.e., PNS convection works to accelerate deleptonization of the PNS. More quantitatively, the core deleptonization rate is roughly two times higher in 3D than in 1D. This can be seen using the electron lepton number (ELN) luminosity displayed in Fig. 19. This phenomenon is mainly due to the fact that PNS convection carries electrons (and ν_e s) from very optically thick regions to the relatively thin regions. We note that at the outer edge of the PNS convective zone most ν_e s are still trapped, but that the lower-energy neutrinos preferentially escape, enhancing deleptonization. We find, however, that the difference in the ELN luminosity between 1D and 3D for the 19– and $25-M_{\odot}$ models moderates with time. This is in part due to the fact that ν_e and $\bar{\nu}_e$ emissions undergo a sharp drop at shock revival. Although there is some progenitor dependence of core deleptonization, we confirm that in general PNS convection accelerates it. This is consistent with the results of previous 2D simulations (Buras et al. 2006).

Figure 20 displays the time evolution of the neutrino luminosity and the average neutrino energies for the 9–,13–,19– and 25 – M_{\odot} progenitors for both 3D and 1D models; the 13 M_{\odot} model is added to this figure to represent non-exploding models. In the early post-bounce phase ($\lesssim 200$ ms), we find that the 3D neutrino luminosities for all species are slightly smaller than in 1D, with the difference being smaller still for the 9 M_{\odot} model. Later, the difference in neutrino luminosity between 1D and 3D depends upon model and species. We now describe the origin of this complexity.

As shown in Figs. 7 and 18, the matter distributions in the envelope of the PNS in 3D are already different from those in 1D, even during the early post-bounce phase ($\lesssim 200$ ms). This affects the locations of the various neutrinospheres and the thermodynamic state of the matter there. As displayed in Fig. 8, the PNS radius in 3D models is systematically larger than in 1D. This would work to increase the

 $^{^3}$ See also the top panels of Fig. 7, which display the same quantities but as a function of radius.

⁴ The electron number can be computed using $\int dM Y_e(M)$, which corresponds to the area in the $Y_e - M$ figure.

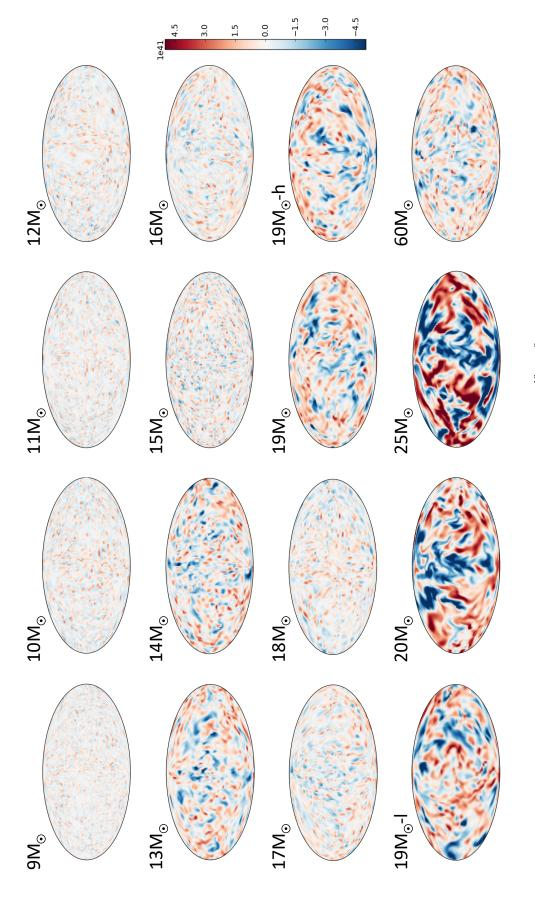


Figure 15. Mollweide projections of the total turbulent energy flux at a radius where $\rho_{\text{ave}} = 5 \times 10^{13} \, \text{g/cm}^3$. This position roughly coincides with the center of PNS convection at 300 ms after bounce. The units are [erg/cm²s]. Note that the greater color contrast indicates a higher variation in the turbulent flux.

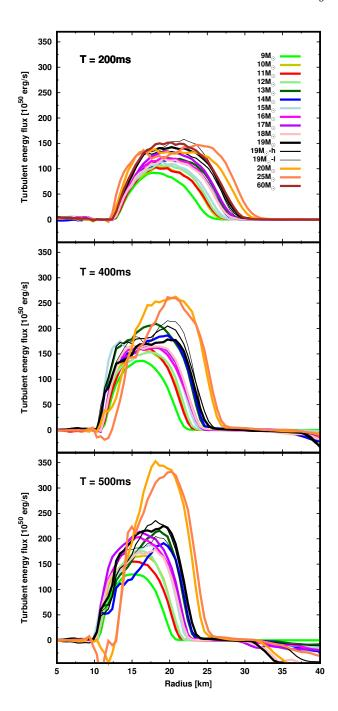


Figure 16. The radial profile of the angle-averaged turbulent energy flux at 200, 400 and 500 ms after bounce from top to bottom, respectively. The results for the $60M_{\odot}$ model are not included in the last two snapshots.

neutrino luminosity, whereas the matter temperature at the neutrinospheres is smaller than in 1D, working to decrease the luminosity⁵. This competition can be characterized very

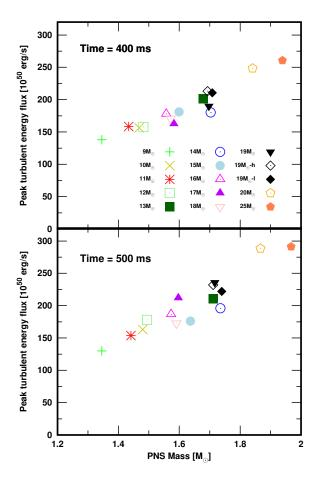


Figure 17. The same as Fig. 12, but for the peak turbulent energy flux.

roughly by a parameter, β , which is defined as

$$\beta \equiv \frac{L_{\nu 3D}}{L_{\nu 1D}} \sim \frac{T_{\nu 3D}^4 R_{\nu 3D}^2}{T_{\nu 1D}^4 R_{\nu 1D}^2},\tag{2}$$

where T_{ν} and R_{ν} denote the matter temperature and radius, respectively, of the neutrinosphere⁶. We find that during the early phase the latter effect dominates the former ($\beta < 1$). As a result, during this early phase the neutrino luminosity is smaller in 3D. Unlike the case for the other species, the production of $\bar{\nu}_e$ s is suppressed by the Fermi degeneracy of the ν_e s. Due to the enhanced supply of leptons by PNS convection, this suppressive effect on the density of $\bar{\nu}_e$ s is stronger in 3D than in 1D (Buras et al. 2006).

At the later phase ($\gtrsim 400$ ms), the difference in neutrino luminosity between 1D and 3D has a different origin than during the earlier phase. The ν_x luminosity in 3D is higher than in 1D for all models, but the differences between 1D and 3D models for the ν_e and $\bar{\nu}_e$ neutrinos depend upon progenitor. The luminosities of the latter species are lower in 3D than 1D for the 19– and 25– M_{\odot} models, but higher in 9 M_{\odot} model. On the other hand, the ν_e and $\bar{\nu}_e$ luminosities

⁵ Consistent with the fact that the matter temperatures in 3D are lower here than in 1D is that the average energy of the neutrinos in 3D is smaller than in 1D (Fig. 20).

⁶ Note that the effect of Fermi degeneracy is not taken into account in Eq. 2 (see e.g., Nagakura et al. (2013)).

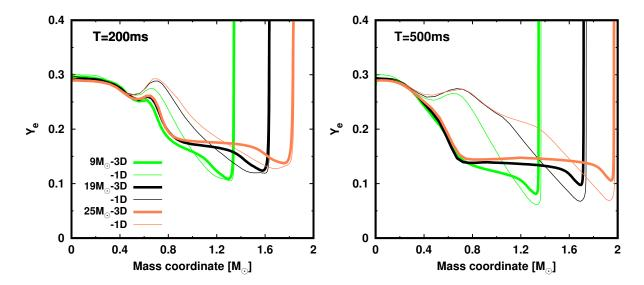


Figure 18. Angle-averaged Y_e profile as a function of enclosed mass for representative 3D models (thick lines). The corresponding profiles obtained from spherically-symmetric simulations (thin lines) are also displayed.

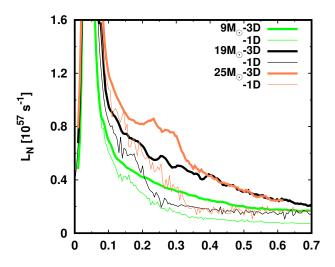


Figure 19. The time evolution of electron-lepton number luminosity for the three selected models.

for the $13 - M_{\odot}$ model depend little on dimension. Such a complex progenitor dependence is due to competing effects.

Unlike during the early post-bounce phase, the effect on the luminosity of the physical expansion of each neutrinosphere as a result of PNS convection dominates that due to the countervailing effect of the corresponding reduction of the matter temperature, i.e., β tends to be greater than unity in the later phase. However, the effect of Fermi degeneracy on the $\bar{\nu}_e$ luminosity mutes the increase in luminosity. Therefore, the net effect of PNS convection on the $\bar{\nu}_e$ luminosity is smaller than that for the other species. This makes subtle the difference between 1D and 3D for the $\bar{\nu}_e$ luminosity and accounts for what we witness for the $9M_{\odot}$

model. Since the accretion component of the neutrino luminosity is negligible at later times due to the swift onset of a vigorous explosion, this conclusion for the $9M_{\odot}$ model is that much more robust. However, the other, more massive, progenitors have higher mass accretion rates (Fig. 2). Thus, effects of the accretion component on the neutrino luminosities is for them of more import. For explosion models (e.g., the 19– and $25-M_{\odot}$ models), the mass accretion rate is reduced by the revival of the shock (Fig. 2). Hence, the accretion component of the neutrino luminosity is reduced substantially. For the ν_e and $\bar{\nu}_e$ neutrinos, this effect overwhelms the increase of the luminosity by PNS convection, which results in a lower luminosity in 3D than in 1D. This conclusion is buttressed by the results for the non-exploding models (e.g., the $13-, 14-, \text{and} 15 - M_{\odot}$ models), in which the difference between 1D and 3D in both the ν_e and $\bar{\nu}_e$ luminosities is smaller than that in the exploding models. On the other hand, the ν_x neutrino luminosity is always higher in 3D than in 1D. This is in part attributed to the fact that the accretion component of the ν_x luminosity is smaller than the diffusion component, regardless of progenitor.

Finally, we discuss the impact of PNS convection on CCSN dynamics. As mentioned above, PNS convection does not much change the luminosity of the ν_e and $\bar{\nu}_e$ neutrinos, but has an influence on their average energies; these are reduced more than 10%. The reduction of these average energies suggests that the efficiency of neutrino heating in the gain region might be reduced, i.e., PNS convection might negatively affect shock revival. However, the enhanced ν_x luminosity accelerates the shrinkage of the PNS itself (Radice et al. 2017) and this effect, like the effect of general relativity (Liebendörfer et al. 2004) and the many-body corrections to the neutrino-matter interaction rates (Burrows et al. 2018), aids explosion. Hence, since there are numerous countervailing effects of PNS convection on core evolution and the neutrino emissions, the actual net impact of PNS convection on the explosion for all progenitor structures is still unclear; a

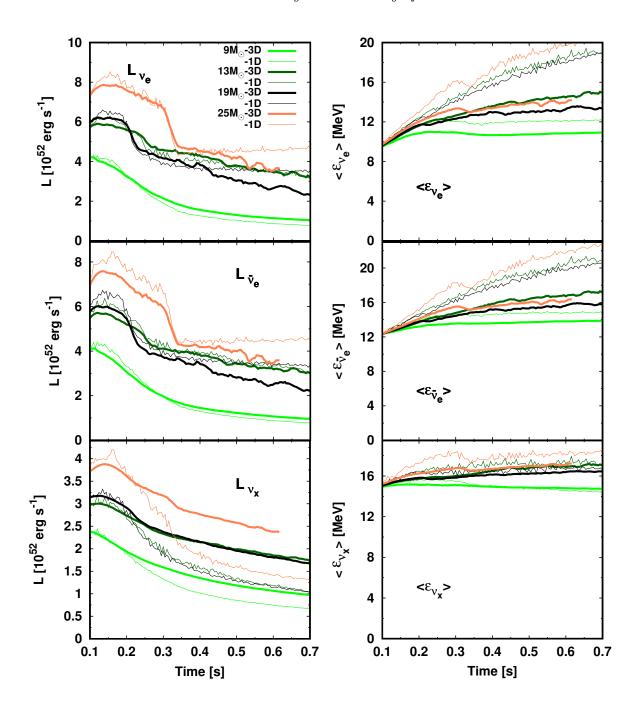


Figure 20. The energy luminosity (left) and average neutrino energy (right) as a function of time for each species of neutrino for four selected models. Note that the $13M_{\odot}$ model represents models that didn't explode in this suite of 3D simulations. The values are taken at 10,000 km.

more detailed study is called for to resolve all the effects, and the net effect, of PNS convection on CCSN dynamics.

4 SUMMARY AND DISCUSSION

In this paper, we have carried out the first systematic study of PNS convection in 3D for a broad and representative range of progenitor masses. We confirm that PNS convection

is a generic, persistent, and important feature of all models and that there is a rich diversity among progenitors. We find in the first ~second after bounce that the overall dynamics and behavior of PNS convection is insensitive to whether the shock is revived. Moreover, we find that the mass of the PNS is the most important quantity that characterizes the vigor of convection and that more massive PNS cores experience more vigorous convection. Moreover, stronger PNS convection results in a physically larger convective layer. We

also find that PNS convection in simulations with different resolutions has similar characteristics. We speculate that at later times (> 1s after core bounce) PNS convection will manifestly differ between models that fail to explode and models that don't, and may be very interestingly different near black hole formation. Longer simulations are definitely required to assess such differences.

We analyzed the characteristics of the turbulence in PNS convection and found that in 3D it deviated from Kolmogorov's theory. Also, we found that the turbulence is anisotropic; indeed the net turbulent energy flux is outgoing and we confirm that PNS convection accelerates the deleptonization of the PNS. The ELN luminosity of the core in 3D is roughly two times higher than that in 1D models (Fig. 19). This is attributed to the fact that PNS convection dredges up leptons to the boundary of the PNS convective zone and, thereby enhances the lepton flux at the outer edge of the PNS. Furthermore, the expanded neutrinospheric radii, accompanied by lower neutrinospheric temperatures compared with those in 1D, accelerates total ELN loss from the PNS. As a result, there are important differences in neutrino emissions between 1D and 3D that also depend strongly on progenitor. Complexity arises, however, from the competition of factors, which we have attempted to clarify in this study.

Although the results presented in this paper are based on a state-of-the-art methodology, uncertainties in some of the input physics, in particular, some neutrino opacities (Burrows et al. 2018) and the nuclear EOS (Roberts et al. 2012; Steiner et al. 2013; Oertel et al. 2017), may affect our findings. As we have observed, PNS convection occurs in the density range of $10^{13} \lesssim \rho \lesssim 10^{14} \, \mathrm{g/cm^3}$, which corresponds to the transition region from inhomogeneous to uniform hadronic matter. In this region, there still remain many ambiguities in both the EOS and the weak-interaction rates. We have not yet determined the sensitivity of PNS convection to these inputs, and doing so should be a goal of future research.

We note that the convective zone in the PNS is an ideal context for the dynamo amplification of magnetic fields, similar to what happens in convective stars and planets. PNS convection persists independent of explosion details and an α^2 and/or $\alpha - \Omega$ (if rotating) dynamo would seem naturally to arise in this generic convective context. Equating 1% of the kinetic energies in the convective layers that we find in our 3D simulations (Fig. 10) to a mean magnetic energy density times the calculated volume of the convective zones reveals that an "equipartition" magnetic field of 10^{12} to 10¹⁵ gauss can easily be accommodated. It can even be larger, but since this region is progressively buried and has a mass cap over it when the neutron star effectively ceases accretion (Burrows et al. 2019a) we might expect the final surface fields to be smaller. Furthermore, generating B-fields in a shell should favor higher-order harmonics locally and the dipole fraction, the one most relevant to pulsar astronomy, is likely subdominant at depth. Therefore, what the surface dipolar moment might be would be an important issue. Finally, the systematics in the vigor and the extent of PNS convection with progenitor structure and PNS mass may point to a corresponding systematics in the B-fields of pulsars born from them. This intriguing possibility, that a pulsar's magnetic fields originates in PNS convection, deserves further scrutiny, but shows promise.

ACKNOWLEDGEMENTS

The authors acknowledge ongoing contributions to this effort by Josh Dolence and Aaron Skinner. We also acknowledge Evan O'Connor regarding the equation of state, Gabriel Martínez-Pinedo concerning electron capture on heavy nuclei, Tug Sukhbold and Stan Woosley for providing details concerning the initial models, Todd Thompson regarding inelastic scattering, and Andrina Nicola for help in computing the turbulent spectrum. We acknowledge support from the U.S. Department of Energy Office of Science and the Office of Advanced Scientific Computing Research via the Scientific Discovery through Advanced Computing (SciDAC4) program and Grant DE-SC0018297 (subaward 00009650). In addition, we gratefully acknowledge support from the U.S. NSF under Grants AST-1714267 and PHY-1144374 (the latter via the Max-Planck/Princeton Center (MPPC) for Plasma Physics). DR cites partial support as a Frank and Peggy Taplin Fellow at the Institute for Advanced Study. An award of computer time was provided by the INCITE program. That research used resources of the Argonne Leadership Computing Facility, which is a DOE Office of Science User Facility supported under Contract DE-AC02-06CH11357. In addition, this overall research project is part of the Blue Waters sustained-petascale computing project, which is supported by the National Science Foundation (awards OCI-0725070 and ACI-1238993) and the state of Illinois. Blue Waters is a joint effort of the University of Illinois at Urbana-Champaign and its National Center for Supercomputing Applications. This general project is also part of the "Three-Dimensional Simulations of Core-Collapse Supernovae" PRAC allocation support by the National Science Foundation (under award #OAC-1809073). Moreover, access under the local award #TG-AST170045 to the resource Stampede2 in the Extreme Science and Engineering Discovery Environment (XSEDE), which is supported by National Science Foundation grant number ACI-1548562, was crucial to the completion of this work. Finally, the authors employed computational resources provided by the TIGRESS high performance computer center at Princeton University, which is jointly supported by the Princeton Institute for Computational Science and Engineering (PIC-SciE) and the Princeton University Office of Information Technology, and acknowledge our continuing allocation at the National Energy Research Scientific Computing Center (NERSC), which is supported by the Office of Science of the US Department of Energy (DOE) under contract DE-AC03-76SF00098.

REFERENCES

Abdikamalov E., et al., 2015, ApJ, 808, 70
Bethe H. A., Wilson J. R., 1985, ApJ, 295, 14
Bonanno A., Urpin V., Belvedere G., 2006, A&A, 451, 1049
Bruenn S. W., 1985, ApJS, 58, 771
Bruenn S. W., Dineva T., 1996, ApJ, 458, L71
Bruenn S. W., Buchler J. R., Livio M., 1979, ApJ, 234, L183
Buras R., Janka H.-T., Rampp M., Kifonidis K., 2006, A&A, 457, 281
Burrows A., Lattimer J. M., 1986, ApJ, 307, 178
Burrows A., Lattimer J. M., 1988, Phys. Rep., 163, 51

Burrows A., Hayes J., Fryxell B. A., 1995, ApJ, 450, 830

- Burrows A., Vartanyan D., Dolence J. C., Skinner M. A., Radice D., 2018, Space Sci. Rev., 214, 33
- Burrows A., Radice D., Vartanyan D., Nagakura H., Skinner M. A., Dolence J., 2019a, arXiv e-prints, p. arXiv:1909.04152
- Burrows A., Radice D., Vartanyan D., 2019b, MNRAS, 485, 3153 Dessart L., Burrows A., Livne E., Ott C. D., 2006, ApJ, 645, 534 Epstein R. I., 1979, MNRAS, 188, 305
- Gessner A., Janka H.-T., 2018, ApJ, 865, 61
- Glas R., Just O., Janka H. T., Obergaulinger M., 2019a, ApJ, 873. 45
- Glas R., Janka H. T., Melson T., Stockinger G., Just O., 2019b, ApJ, 881, 36
- Gossan S. E., Fuller J., Roberts L. F., 2019, arXiv e-prints, p. arXiv:1910.07599
- Guilet J., Müller E., Janka H.-T., 2015, $\underline{\mathsf{MNRAS}},\,447,\,3992$
- Keil W., Janka H. T., Mueller E., 1996, $\ensuremath{\mathsf{ApJ}}\xspace,\,473,\,L111$
- Kitaura F. S., Janka H. T., Hillebrandt W., 2006, A&A, 450, 345
 Kuroda T., Kotake K., Takiwaki T., Thielemann F.-K., 2018,
 MNRAS, 477, L80
- Lattimer J. M., Mazurek T. J., 1981, ApJ, 246, 955
- Lattimer J. M., Prakash M., 2000, Phys. Rep., 333, 121
- Lentz E. J., et al., 2015, ApJ, 807, L31
- Liebendörfer M., Mezzacappa A., Messer O. E. B., Martinez-Pinedo G., Hix W. R., Thielemann F.-K., 2003, Nuclear Physics A, 719, C144
- Liebendörfer M., Messer O. E. B., Mezzacappa A., Bruenn S. W., Cardall C. Y., Thielemann F.-K., 2004, ApJS, 150, 263
- Livio M., Buchler J. R., Colgate S. A., 1980, ApJ, 238, L139
- Melson T., Janka H. T., 2019, arXiv e-prints, p. arXiv:1904.01699
 Mezzacappa A., Calder A. C., Bruenn S. W., Blondin J. M.,
 Guidry M. W., Strayer M. R., Umar A. S., 1998, ApJ, 493,
- Morozova V., Radice D., Burrows A., Vartanyan D., 2018, ApJ, 861, 10
- Müller B., Janka H.-T., 2015, MNRAS, 448, 2141
- Müller B., et al., 2019, MNRAS, 484, 3307
- Nagakura H., Yamamoto Y., Yamada S., 2013, ApJ, 765, 123
- Nagakura H., Burrows A., Radice D., Vartanyan D., 2019a, MNRAS, p. 2343
- Nagakura H., Furusawa S., Togashi H., Richers S., Sumiyoshi K., Yamada S., 2019b, ApJS, 240, 38
- Nagakura H., Sumiyoshi K., Yamada S., 2019c, ApJ, 880, L28
- Nakamura K., Horiuchi S., Tanaka M., Hayama K., Takiwaki T., Kotake K., 2016, MNRAS, 461, 3296
- O'Connor E. P., Couch S. M., 2018, ApJ, 865, 81
- Oertel M., Hempel M., Klähn T., Typel S., 2017, Reviews of Modern Physics, 89, 015007
- Ott C. D., Roberts L. F., da Silva Schneider A., Fedrow J. M., Haas R., Schnetter E., 2018, ApJ, 855, L3
- Pan K.-C., Liebendörfer M., Couch S. M., Thielemann F.-K., 2018, Astrophys. J., 857, 13
- Powell J., Müller B., 2019, MNRAS, 487, 1178
- Radice D., Burrows A., Vartanyan D., Skinner M. A., Dolence J. C., 2017, ApJ, 850, 43
- Radice D., Morozova V., Burrows A., Vartanyan D., Nagakura H., 2019, ApJ, 876, L9
- Roberts L. F., Shen G., Cirigliano V., Pons J. A., Reddy S., Woosley S. E., 2012, Phys. Rev. Lett., 108, 061103
- Roberts L. F., Ott C. D., Haas R., O'Connor E. P., Diener P., Schnetter E., 2016, ApJ, 831, 98
- Schneider A. S., Roberts L. F., Ott C. D., O'connor E., 2019, arXiv e-prints, p. arXiv:1906.02009
- Skinner M. A., Burrows A., Dolence J. C., 2016, ApJ, 831, 81
- Skinner M. A., Dolence J. C., Burrows A., Radice D., Vartanyan D., 2019, The Astrophysical Journal Supplement Series, 241, 7
- Sotani H., Sumiyoshi K., 2019, arXiv e-prints, p. arXiv:1909.11816

- Steiner A. W., Hempel M., Fischer T., 2013, ApJ, 774, 17
 Sukhbold T., Ertl T., Woosley S. E., Brown J. M., Janka H. T., 2016, ApJ, 821, 38
- Sukhbold T., Woosley S. E., Heger A., 2018, ApJ, 860, 93
- Sumiyoshi K., Yamada S., Suzuki H., Chiba S., 2006, Phys. Rev. Lett., 97, 091101
- Takiwaki T., Kotake K., Suwa Y., 2014, ApJ, 786, 83
- Tamborra I., Hanke F., Janka H.-T., Müller B., Raffelt G. G., Marek A., 2014, ApJ, 792, 96
- Thompson C., Duncan R. C., 1993, ApJ, 408, 194
- Torres-Forné A., Cerdá-Durán P., Obergaulinger M., Müller B., Font J. A., 2019, Phys. Rev. Lett., 123, 051102
- Vartanyan D., Burrows A., Radice D., Skinner M. A., Dolence J., 2018, MNRAS, 477, 3091
- Vartanyan D., Burrows A., Radice D., Skinner M. A., Dolence J., 2019a, MNRAS, 482, 351
- Vartanyan D., Burrows A., Radice D., 2019b, MNRAS, 489, 2227
 Walk L., Tamborra I., Janka H.-T., Summa A., 2019a, arXiv e-prints, p. arXiv:1901.06235
- Walk L., Tamborra I., Janka H.-T., Summa A., 2019b, arXiv e-prints, p. arXiv:1910.12971
- Wilson J. R., Mayle R. W., 1988, Phys. Rep., 163, 63 van den Horn L. J., van Weert C. G., 1984, A&A, 136, 74
- This paper has been typeset from a T_EX/I_EX file prepared by the author.